Engineering of metal-clad optical nanocavity to optimize coupling with integrated waveguides

Myung-Ki Kim,[1,3] Zheng Li,[1,3] Kun Huang,[1] Ryan Going,[2] Ming C. Wu,[2] and Hyuck Choo[1,*]

[1]*The Moore Laboratory, Electrical Engineering, California Institute of Technology, Pasadena, CA 91125, USA*
[2]*Electrical Engineering & Computer Sciences, Cory Hall, UC Berkeley, Berkeley, CA 94720, USA*
[3]*These authors contributed equally to this work*
[*]*hchoo@caltech.edu*

Abstract: We propose a cladding engineering method that flexibly modifies the radiation patterns and rates of metal-clad nanoscale optical cavity. Optimally adjusting the cladding symmetry of the metal-clad nanoscale optical cavity modifies the modal symmetry and produces highly directional radiation that leads to 90% coupling efficiency into an integrated waveguide. In addition, the radiation rate of the cavity mode can be matched to its absorption rate by adjusting the thickness of the bottom-cladding layer. This approach optimizes the energy-flow rate from the waveguide and maximizes the energy confined inside the nanoscale optical cavity.

OCIS codes: (250.5300) Photonic integrated circuits; (250.5403) Plasmonics.

References and links

1. B. Razavi, Design of integrated circuits for optical communications (McGraw-Hill, New York, 2002).
2. V. R. Almeida, C. A. Barrios, R. R. Panepucci, and M. Lipson, "All-optical control of light on a silicon chip," Nature **431**(7012), 1081–1084 (2004).
3. L. Liao, A. Liu, J. Basak, H. Nguyen, M. Paniccia, D. Rubin, Y. Chetrit, R. Cohen, and N. Izhaky, "40 Gbit/s silicon optical modulator for high-speed applications," Electron. Lett. **43**(22), 1196 (2007).
4. S. Fama, L. Colace, G. Masini, G. Assanto, and H.-C. Luan, "High performance germanium-on-silicon detectors for optical communications," Appl. Phys. Lett. **81**(4), 586–588 (2002).
5. A. W. Fang, H. Park, O. Cohen, R. Jones, M. J. Paniccia, and J. E. Bowers, "Electrically pumped hybrid AlGaInAs-silicon evanescent laser," Opt. Express **14**(20), 9203–9210 (2006).
6. J. Van Campenhout, P. Rojo Romeo, P. Regreny, C. Seassal, D. Van Thourhout, S. Verstuyft, L. Di Cioccio, J.-M. Fedeli, C. Lagahe, and R. Baets, "Electrically pumped InP-based microdisk lasers integrated with a nanophotonic silicon-on-insulator waveguide circuit," Opt. Express **15**(11), 6744–6749 (2007).
7. D. Liang, M. Fiorentino, T. Okumura, H.-H. Chang, D. T. Spencer, Y.-H. Kuo, A. W. Fang, D. Dai, R. G. Beausoleil, and J. E. Bowers, "Electrically-pumped compact hybrid silicon microring lasers for optical interconnects," Opt. Express **17**(22), 20355–20364 (2009).
8. J. Van Campenhout, P. R. A. Binetti, P. R. Romeo, P. Regreny, C. Seassal, X. J. M. Leijtens, T. de Vries, Y. S. Oei, R. P. J. van Veldhoven, R. Notzel, L. É. Di Cioccio, J.-M. Fedeli, M. K. Smit, D. Van Thourhout, and R. Baets, "Low-Footprint Optical Interconnect on an SOI Chip Through Heterogeneous Integration of InP-Based Microdisk Lasers and Microdetectors," IEEE Photon. Technol. Lett. **21**(8), 522–524 (2009).
9. G. Roelkens, L. Liu, D. Liang, R. Jones, A. W. Fang, B. Koch, and J. E. Bowers, "III-V/silicon photonics for on-chip and intra-chip optical interconnects," Laser Photon. Rev. **4**(6), 751–779 (2010).
10. L. C. Kimerling, D. Ahn, A. B. Apsel, M. Beals, D. Carothers, Y.-K. Chen, T. Conway, D. M. Gill, M. Grove, C.-Y. Hong, M. Lipson, J. Liu, J. Michel, D. Pan, S. S. Patel, A. T. Pomerene, M. Rasras, D. K. Sparacin, K.-Y. Tu, A. E. White, and C. W. Wong, "Electronic-photonic integrated circuits on the CMOS platform," Proc. SPIE **6125**, 612502, 612502-10 (2006).
11. J. S. Orcutt, A. Khilo, M. A. Popovic, C. W. Holzwarth, B. Moss, and M. S. Hanqing Li, Dahlem, T.D. Bonifield, F.X. Kartner, E.P. Ippen, J.L. Hoyt, R.J. Ram, and V. Stojanovic, "Demonstration of an electronic photonic integrated circuit in a commercial scaled bulk CMOS process," Proc. Conf. Lasers and Electro-Optics (CLEO) (2008).
12. W. L. Barnes, A. Dereux, and T. W. Ebbesen, "Surface plasmon subwavelength optics," Nature **424**(6950), 824–830 (2003).
13. M. T. Hill, Y.-S. Oei, B. Smalbrugge, Y. Zhu, T. de Vries, P. J. van Veldhoven, F. W. M. van Otten, T. J. Eijkemans, J. P. Turkiewicz, H. de Waardt, E. J. Geluk, S.-H. Kwon, Y.-H. Lee, R. Notzel, and M. K. Smit, "Lasing in metallic-coated nanocavities," Nat. Photonics **1**(10), 589–594 (2007).

#191484 - $15.00 USD Received 5 Jun 2013; revised 19 Sep 2013; accepted 11 Oct 2013; published 22 Oct 2013

14. D. J. Bergman and M. I. Stockman, "Surface Plasmon Amplification by Stimulated Emission of Radiation: Quantum Generation of Coherent Surface Plasmons in Nanosystems," Phys. Rev. Lett. **90**(2), 027402 (2003).
15. H. T. Miyazaki and Y. Kurokawa, "Squeezing Visible Light Waves into a 3-nm-Thick and 55-nm-Long Plasmon Cavity," Phys. Rev. Lett. **96**(9), 097401 (2006).
16. M. T. Hill, M. Marell, E. S. P. Leong, B. Smalbrugge, Y. Zhu, M. Sun, P. J. van Veldhoven, E. J. Geluk, F. Karouta, Y.-S. Oei, R. Nötzel, C.-Z. Ning, and M. K. Smit, "Lasing in metal-insulator-metal sub-wavelength plasmonic waveguides," Opt. Express **17**(13), 11107–11112 (2009).
17. M. A. Noginov, G. Zhu, A. M. Belgrave, R. Bakker, V. M. Shalaev, E. E. Narimanov, S. Stout, E. Herz, T. Suteewong, and U. Wiesner, "Demonstration of a spaser-based nanolaser," Nature **460**(7259), 1110–1112 (2009).
18. R. F. Oulton, V. J. Sorger, T. Zentgraf, R.-M. Ma, C. Gladden, L. Dai, G. Bartal, and X. Zhang, "Plasmon lasers at deep subwavelength scale," Nature **461**(7264), 629–632 (2009).
19. M. P. Nezhad, A. Simic, O. Bondarenko, B. Slutsky, A. Mizrahi, L. Feng, V. Lomakin, and Y. Fainman, "Room-temperature subwavelength metallo-dielectric lasers," Nat. Photonics **4**(6), 395–399 (2010).
20. S.-H. Kwon, J.-H. Kang, C. Seassal, S.-K. Kim, P. Regreny, Y.-H. Lee, C. M. Lieber, and H.-G. Park, "Subwavelength plasmonic lasing from a semiconductor nanodisk with silver nanopan cavity," Nano Lett. **10**(9), 3679–3683 (2010).
21. M.-K. Kim, S. H. Lee, M. Choi, B.-H. Ahn, N. Park, Y.-H. Lee, and B. Min, "Low-loss surface-plasmonic nanobeam cavities," Opt. Express **18**(11), 11089–11096 (2010).
22. K. Yu, A. Lakhani, and M. C. Wu, "Subwavelength metal-optic semiconductor nanopatch lasers," Opt. Express **18**(9), 8790–8799 (2010).
23. J. H. Lee, M. Khajavikhan, A. Simic, Q. Gu, O. Bondarenko, B. Slutsky, M. P. Nezhad, and Y. Fainman, "Electrically pumped sub-wavelength metallo-dielectric pedestal pillar lasers," Opt. Express **19**(22), 21524–21531 (2011).
24. S.-H. Kim, J. Huang, and A. Scherer, "From vertical-cavities to hybrid metal/photonic-crystal nanocavities: towards high-efficiency nanolasers," J. Opt. Soc. Am. B **29**(4), 577–588 (2012).
25. K. Ding and C. Z. Ning, "Metallic subwavelength-cavity semiconductor nanolasers," Light: Sci. Appl. **1**(7), e20 (2012), doi:10.1038/lsa.2012.20.
26. M.-K. Kim, A. M. Lakhani, and M. C. Wu, "Efficient waveguide-coupling of metal-clad nanolaser cavities," Opt. Express **19**(23), 23504–23512 (2011).
27. K. Vahala, *Optical Microcavities* (World Scientific, Singapore, 2004).
28. G.-H. Kim, Y.-H. Lee, A. Shinya, and M. Notomi, "Coupling of small, low-loss hexapole mode with photonic crystal slab waveguide mode," Opt. Express **12**(26), 6624–6631 (2004).
29. H. Haus, *Waves and Fields in Optoelectronics* (Prentice-Hall, New Jersey, 1984).

1. Introduction

Telecommunication networks, data-storage centers, and many other integrated photonic systems continue to evolve and demand faster, more compact and more energy-efficient on-chip optical communication devices [1–4]. From among the available device-implementation approaches, the silicon/III-V hybrid approach has become a popular choice for implementing large-scale integrated on-chip photonic components because the hybrid approach allows the advantages of both the silicon (Si) and III-V approaches to be exploited in a complementary way [2–11]. In the hybrid approach, the favorable optical properties of Si in the telecommunication-wavelength region and the well-established processing technologies and infrastructure of the Si industry are effectively combined with the active functions of integrated III-V components for light generation, detection, and modulation. In addition, by reducing the physical dimensions and mode volumes of III-V active components to the scale of a wavelength, the performance metrics of the hybrid devices have been continuously improved without significantly degrading desirable optical properties such as a high cavity quality factor Q and an effective energy confinement in the active III-V materials [5–8].

Since improving the performance of optical communication is always in demand, further reducing the size of III-V components down to the subwavelength scale is necessary. However, because of the optical diffraction limit, further reducing the size of conventional III-V components does not generate the expected advantages [12]. To overcome this limitation, researchers have recently explored metallic III-V nanoscale optical cavities and achieved physical and modal sizes on the subwavelength scale, which is sufficiently small to open up new possibilities for implementing higher-performing Si/III-V hybrid optical systems [13–25]. However, with this approach, one significant problem in practical integration and use arises: Because of the extremely small output aperture of such a cavity, the radiation from the cavity diverges very rapidly, which makes optical coupling between the III-V cavity and

#191484 - $15.00 USD Received 5 Jun 2013; revised 19 Sep 2013; accepted 11 Oct 2013; published 22 Oct 2013

integrated Si-waveguides very inefficient [25,26]. To implement practical devices, a more efficient coupling method is highly desired.

In this work, we propose a straightforward radiation-engineering method that could greatly enhance the optical coupling between a metal-clad nanoscale optical cavity (or nanocavity) and an integrated bidirectional or unidirectional waveguide. Varying the thicknesses of the intermediate dielectric cladding layers between the III-V nanocavity and the metal shell breaks the rotational and mirror symmetry of the fundamental transverse-electric (TE) mode of the III-V nanocavity. By using this phenomenon, we engineer and generate radiation patterns of the III-V metal nanocavity that result in highly directional far-field radiation patterns and thereby strongly enhance the output coupling efficiency (~90%) into an integrated bidirectional or unidirectional Si waveguide. In addition, to maximize the energy confined in the III-V cavity, we adjust the height of the bottom-cladding layer to tune the radiation rate of the cavity mode so that it matches its absorption rate. At this optimal radiation rate, the proper amount of light couples from the waveguide into the nanocavity, and the energy inside the cavity is maximized. We strongly believe our efficient coupling technique between metal-clad III-V nanocavities and integrated Si photonic devices will create new possibilities for implementing ultra-compact, extremely fast, energy-efficient Si/III-V integrated optical communication devices.

2. Far-field engineering of metal-clad nanocavity

A schematic of a simplified metal-clad III-V nanocavity (without Si integration) is presented in Fig. 1(a). The device is composed of three major parts: (1) the 350 nm × 350 nm × 350 nm III-V (InGaAsP) nanocavity, (2) the low-refractive-index SiO_2 cladding layer that wraps around the III-V cavity, and (3) the 100-nm-thick silver layer that coats the cladding layers everywhere except on the bottom, which serves to couple with air. The cavity supports the fundamental TE mode with a doughnut profile (a monopole-like mode) at a telecommunication frequency near 200 THz. The thicknesses of the cladding layers along the x and y directions [a, b_1, and b_2 defined in Fig. 1(b)] are adjusted to generate the desired radiation patterns. The top and bottom cladding layers above and below the III-V cavity are fixed at 150 and 350 nm, respectively.

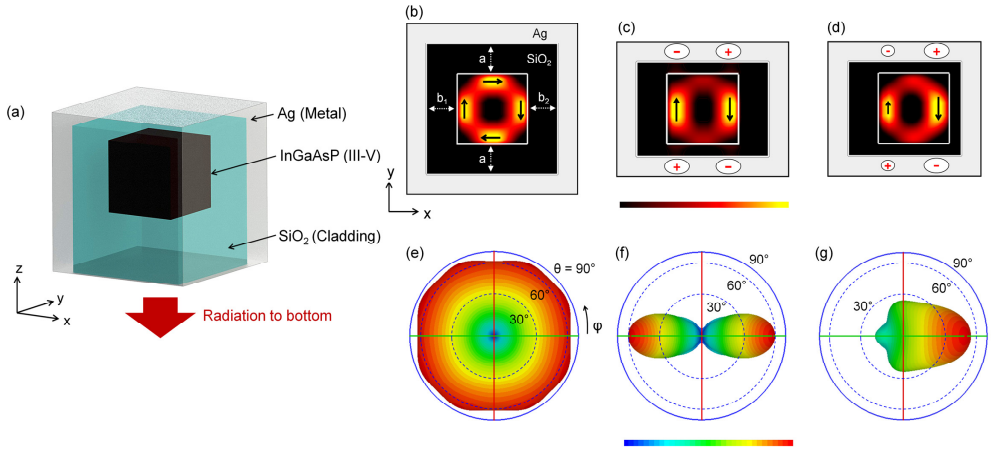

Fig. 1. (a) Schematic of metallic III-V cubic nanocavity. Energy-density distributions (major electric field arrows overlaid) and corresponding far-field radiation patterns in the $-z$ direction for (b, e) cladding layers $a = b_1 = b_2 = 150$ nm around the III-V cubic nanocavity, (c, f) $a = 60$ nm, $b_1 = b_2 = 150$ nm, and (d, g) $a = 60$ nm, $b_1 = 150$ nm, $b_2 = 60$ nm.

For the cladding layer, it is important to use a low-index material because it helps overcome dissipative absorption losses in the metal and increases the cavity Q factor [19]. Having the same cladding thickness in the x and y directions ($a = b_1 = b_2$) increases the Q

#191484 - $15.00 USD Received 5 Jun 2013; revised 19 Sep 2013; accepted 11 Oct 2013; published 22 Oct 2013

factor without significantly affecting the original mode profile, mode volume, and resonant frequency. From our simulation, we find that the Q factor is maximized to 2010 for a cladding thickness of 150 nm, which is much higher than the Q factor of 10 for the III-V nanocavity with the same dimensions but without the metal-clad enclosure. For a nanocavity with a metal shell but without the cladding layers, the Q factor attains a maximum of about 208. To maximize the cavity Q factor in the metal-clad semiconductor nanocavity, it is necessary to find a cladding thickness that maintains the proper balance between absorption and radiation losses.

We start engineering the cladding by considering a symmetric metal-clad nanocavity. For our simulation, we used a finite-difference time-domain (FDTD) commercial simulator provided by Lumerical©. To excite the cavity mode, we placed inside the cavity Gaussian-shaped, time-dependent dipole sources with a very short duration (much shorter than the lifetime of the cavity mode), and under the excitation conditions, the source position has minimal effect on the properties of the cavity mode. Figure 1(b) shows the energy-density distribution and major electric field directions of the cavity mode along the *x*-*y* cross-sectional plane when $a = b_1 = b_2 = 150$ nm. This figure shows that the mode profile still strongly resembles that of the original fundamental dielectric TE mode. The mode volume and the resonant frequency are calculated to be 0.26 $(\lambda/n)^3$, and 206.2 THz, respectively, and the *n* in the mode volume expression stands for the refractive index of the nanocavity, which is InGaAsP in this case. Next, we obtained the far-field radiation pattern of the mode profile, which is shown in Fig. 1(e), by projecting the emission from the cavity toward the bottom of the device (i.e., in the −z direction). If the structural geometry of the III-V nanocavity exhibits 90°-rotation symmetry along the x-y plane, please note that the far-field intensity pattern also preserves the 90°-rotation symmetry of the near-field intensity patterns. This symmetric, nearly omnidirectional radiation pattern makes coupling from the cavity into an integrated waveguide very inefficient and is one of the biggest obstacles to implementing practical Si/III-V integrated nanoscale devices that involve metal-clad semiconductor nanocavities.

By breaking the rotational symmetry of the cavity mode, however, we can engineer and produce desired far-field radiation patterns in preferred directions and enhance their coupling into integrated waveguides. There are two possible ways to break the symmetry: (1) deform the overall geometry of the III-V cavity or (2) vary the thickness of the cladding layer on each of the four vertical surfaces of the III-V nanocavity. Here, we use the latter approach because the geometric deformation of the original III-V cavity structure would lead to other undesirable consequences such as large resonance shifts, *Q*-factor fluctuation, and potential fabrication challenges. Compared to method (1) (i.e., deforming the geometry of the cavity itself), cladding engineering of metal-clad nanocavities is preferred because the cladding-layer thickness heavily influences the strength of surface-plasmon-polariton (SPP) coupling between the III-V cavity and the outer metal shell, thereby influencing the formation of the final cavity mode.

We start by partially breaking the 90°-rotation symmetry in the *x*-*y* plane of the metal-clad cavity by introducing thinner cladding layers along the *y* direction. Figure 1(c) shows the physical geometry of the metal-clad nanocavity and the energy-density profile and dominant electric fields in the modified cavity mode when $a < b_1 = b_2$, where *a*, b_1, and b_2 are 60, 150, and 150 nm, respectively. The energy distribution in Fig. 1(c) shows that the 90°-rotation symmetry of the near-field intensity profile is broken and that the electric field along the *y* direction becomes dominant because of the stronger SPP interaction in the *y* direction. Since the radiation of the electric fields in the *y*-direction, if treated as dipole distributions in the first-order approximation, mainly contribute to the far-field radiations in the *x*-direction, this enhancement, which originates from the thinner cladding layers along the same *y* direction, makes the *x*-direction *k* component (or k_x) of the cavity mode dominant and strongly amplifies the far-field radiation along the *x* direction, as shown in Fig. 1(f). This stretching results in about 80% of the radiation power being concentrated within $\varphi = \pm 30°$ [φ is defined in Fig. 1(e)] from the *x* axis. The *Q* factor is calculated to be 1200, which is degraded from 2010.

#191484 - $15.00 USD Received 5 Jun 2013; revised 19 Sep 2013; accepted 11 Oct 2013; published 22 Oct 2013

This decrease in Q is caused by increased metal absorption due to the thinner cladding layers along the y direction. The mode volume is calculated to be 0.24 $(\lambda/n)^3$.

Next, to generate unidirectional far-field radiation patterns, we take another step to break the remaining mirror symmetry with respect to the y-z plane at the center of the cavity shown in Fig. 1(c). This is accomplished in a manner similar to that used to break the 90°-rotation symmetry; namely, by assigning a different thickness to the cladding layer on each of the two vertical surfaces in the x direction (i.e., $b_1 \neq b_2$). Figure 1(d) shows the energy-density distribution and the dominant electric fields of the cavity mode cases where b_1 (left side) > b_2 (right side), and a, b_1, and b_2 are 60, 150, and 60 nm, respectively. The electric field is still oriented primarily in the y direction, which implies that the majority of the k vectors are still orientated in the x direction, with the near-field intensity pattern strongly biased toward the + x direction, as shown in Fig. 1(d). This directionally biased near-field pattern generates unidirectional radiation from the metal-clad III-V nanocavity with about 70% of the power radiating in the + x direction [Fig. 1(g)]. This strong directional bias results from the different SPP-coupling strengths between the left and right sides of the cavity, which in turn results from asymmetric charge accumulations, as shown in Fig. 1(d). Thus, simple cladding engineering within the boundary conditions $a \leq b_1 < b_2$ allows us to adjust the far-field radiation pattern along the + x direction. The Q factor and the mode volume are calculated to be 950 and 0.26 $(\lambda/n)^3$, respectively.

3. Optimization of coupling efficiency in III-V/Si hybrid system

The cladding-engineering technique discussed with the help of Fig. 1 can be applied to enhance bidirectional or unidirectional coupling between the metallic III-V nanocavity and the Si waveguide in integrated Si/III-V devices. Figures 2(a) and 2(b) present a schematic of the proposed metal-clad III-V nanocavities integrated on top of bidirectional and unidirectional, single-mode silicon-on-insulator (SOI) waveguide, respectively. The III-V nanocavity consists of an InGaAsP bulk semiconductor cube with the same dimensions of 350 nm × 350 nm × 350 nm as for Fig. 1(a). The device is designed for electrical carrier injection, and so includes doped InP posts on the top and bottom of the cavity. More structural details of the device illustrated in Fig. 2 are provided in [26].

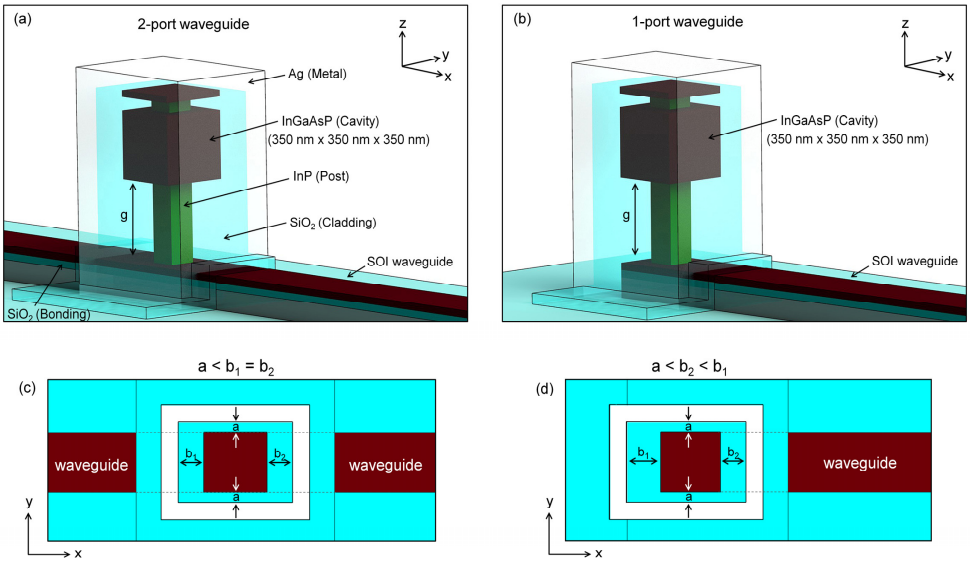

Fig. 2. (a, b) Perspective and (c, d) cross-sectional schematic views of metal-clad III-V nanocavities integrated onto a bidirectional and unidirectional silicon-on-insulator waveguide.

#191484 - $15.00 USD Received 5 Jun 2013; revised 19 Sep 2013; accepted 11 Oct 2013; published 22 Oct 2013

We first examine the case in which a metal-clad III-V nanocavity couples with a bidirectional Si waveguide, which is shown in Figs. 2(a) and 2(c). Continuing from our earlier analysis for Figs. 1(c) and 1(f), we introduce cladding layers that are thinner in the y direction than in the x direction [$a < b_1 = b_2$, where a, b_1, and b_2 are defined in Fig. 2(c)] to break the 90°-rotation symmetry in the x-y plane of the metal-clad nanocavity and enhance coupling from the nanocavity to the bidirectional waveguide. Figure 3(a) shows the coupling efficiency as a function of the difference between the cladding thicknesses in the x and y directions. Here, we fix both b_1 and b_2 at 150 nm and vary a. The coupling efficiency $\eta = \gamma_{waveguide} / \gamma_{rad}$, which is the power flowing from the cavity mode to the waveguide, is defined as the ratio between the cavity-to-waveguide coupling rate $\gamma_{waveguide}$ and directly calculated from power integration in the FDTD software. And, the total cavity-radiation rate γ_{rad}, which is the power loss of the cavity mode except the metallic loss, is obtained from the Q-factor calculations, as described in [26] with more details. Note that the coupling efficiency η does not depend on the total energy stored by the cavity mode, to which both $\gamma_{waveguide}$ and γ_{rad} are proportional. For $a = b_1 = b_2 = 150$ nm, the observed coupling efficiency is only 27%. When a is reduced below 60 nm, the coupling efficiency jumps to near 80% (corresponding to $Q < 1040$), as shown in Fig. 3(a), because the cavity mode is dominated by k_x so the radiation in the x direction dominates. The smaller a results in a lower Q factor due to enhanced SPP coupling with the metal, which leads to greater absorption losses. Figure 3(b) shows the intensity profile (logarithmic scale) of the electric field along the cross-sectional x-z plane at the center of the cavity and illustrates how much energy couples into the bidirectional Si waveguide from the metal-clad III-V nanocavity with the optimal cladding thicknesses ($a = 60$ nm, $b_1 = b_2 = 150$ nm). The inset of Fig. 3(b) shows the energy-density distribution along the x-y plane at the center of the cavity. Thus, the field intensity is primarily oriented along the y direction, similarly to the results shown in Fig. 1(c). Figure 3(c) shows the far-field radiation pattern in the bottom direction ($-z$ direction) resulting from Fig. 3(b).

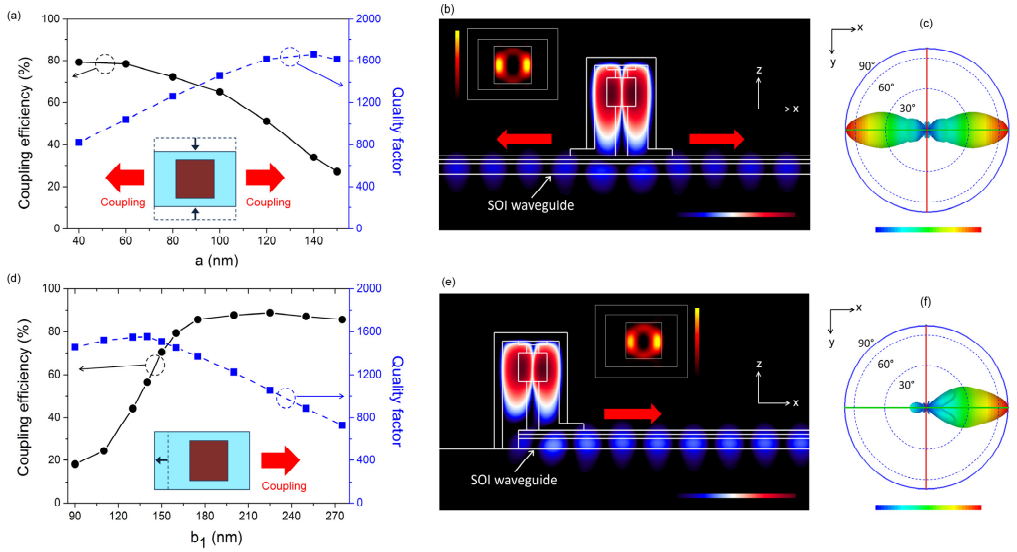

Fig. 3. (a, d) Coupling efficiencies and Q factors as a function of a and b_1 in a metal-clad III-V cavity coupled with bidirectional and unidirectional Si waveguide, respectively. In the bidirectional case, b_1 and b_2 are fixed at 150 nm and, in the unidirectional case, a and b_2 are fixed at 90 and 150 nm, respectively. (b, e) Profiles of E^2 on logarithmic scale along x-z plane (in the bidirectional case, $a = 60$ nm, in the unidirectional case, $b_1 = 180$ nm): Insets show the energy-density profiles along the x-y plane at the center of cavity. (c, f) Far-field patterns toward bottom direction ($-z$ direction) calculated right above the waveguide, for the cases given for panels (b) and (e), respectively.

#191484 - $15.00 USD Received 5 Jun 2013; revised 19 Sep 2013; accepted 11 Oct 2013; published 22 Oct 2013

For unidirectional coupling [Figs. 2(b) and 2(d)], we enhance the unidirectionality by making $b_1 > b_2$, which breaks the mirror symmetry with respect to the *y*-*z* plane at the center of the cavity, very similar to the case described for Figs. 1(d) and 1(g). Figure 3(d) shows the coupling efficiency as a function of b_1 with *a* and b_2 fixed at 90 and 150 nm, respectively. As expected, a large asymmetry ratio between b_1 and b_2 highly enhances coupling into the unidirectional waveguide, and its efficiency increases up to 90%. When b_1 exceeds 140 nm, the *Q* factor starts to degrade significantly because of the increased cavity-to-waveguide rate $\gamma_{waveguide}$ and total cavity-radiation rate γ_{rad}. For the optimal case in which the coupling efficiency is near maximum while the Q factor still remains relatively high, b_1 = 180 nm, and the corresponding coupling efficiency and *Q* factor are calculated to be 86% and 1350, respectively. Interestingly, when b_1 exceeds 180 nm, the total area of the cavity contacting the waveguide underneath becomes larger and, thus, the radiation rate increases while the Q factor lowers. When this happens, the coupling efficiency tends to remain constant, ranging between 85% and 90%, which indicates that the energy is still efficiently flowing into the waveguides rather than leaking into the substrate. Figure 3(e) shows the intensity profile of the electric field along the *x*-*z* plane at the cavity center for *a* = 90 nm, b_1 = 180 nm, and b_2 = 150 nm and illustrates how much energy couples from the metal-clad III-V nanocavity into the integrated unidirectional Si waveguide under optimal cladding conditions. The inset of Fig. 3(e) shows the energy-density distribution along the *x*-*y* plane at the center of cavity, which represents the near-field intensity strongly biased in the + *x* direction, similar to Fig. 1(d). Figure 3(f) shows the far-field radiation pattern in the bottom direction (–*z*) of the nanocavity resulting from Fig. 3(e). In both the bidirectional and unidirectional cases, it is quite clear how effectively our cladding engineering could improve the coupling from the metal-clad III-V nanocavity into integrated bidirectional or unidirectional waveguides.

4. Optimization of cavity-energy in III-V/Si hybrid system

Finally, we discuss how to maximize the amount of energy confined inside the metal-clad III-V nanocavity when light couples from the integrated Si waveguide into the nanocavity. This study is particularly relevant to maximizing the performance of nanodetectors and modulators implemented using the Si/III-V hybrid approach. If the cavity couples with a waveguide in the weak-evanescent-coupling regime, the amount of energy in the cavity depends theoretically on the ratio of the radiation and absorption rates of the cavity mode to the cavity-to-waveguide coupling efficiency [27]. In addition, the cavity-waveguide distance generally serves as a means to control the radiation rate γ_{rad} and the coupling rate $\gamma_{waveguide}$ of the cavity mode [28]. Similarly, in the proposed structure shown in Figs. 2(a) and 2(b), the thickness of the bottom cladding layer (or the height *g* of the bottom InP post) can also be used to control γ_{rad} and $\gamma_{waveguide}$.

First, we examine how the coupling efficiencies and the cavity *Q* factors vary as a function of *g* with optimized dimensions (1) for the unidirectional-waveguide case (η_{uni}, Q_{uni}) where *a* = 90 nm, b_1 = 180 nm, and b_2 = 150 nm and (2) for the bidirectional-waveguide case (η_{bi}, Q_{bi}) where *a* = 60 nm, $b_1 = b_2$ = 150 nm, as shown in Fig. 4(a). In this figure, η_{uni} and η_{bi} remain constant between about 82% and 87% and between about 77% and 79%, respectively, as *g* varies between 200 and 600 nm. This implies that the two rates γ_{rad} and $\gamma_{waveguide}$ increase almost at the same rate so that the ratio $\gamma_{waveguide} / \gamma_{rad}$ remains constant as *g* is reduced for both the unidirectional ($\gamma_{rad,uni}$, $\gamma_{waveguide,uni}$) and bidirectional ($\gamma_{rad,bi}$, $\gamma_{waveguide,bi}$) cases. We attribute the degradation of *Q* with the reduction of *g* to the increase in γ_{rad}. The cavity-to-metal absorption rates $\gamma_{abs,uni}$ and $\gamma_{abs,bi}$ for the unidirectional and bidirectional cases, respectively, remain mostly constant because of the fixed cladding thickness along the *x* and *y* directions (fixed *a*, b_1, and b_2). Figure 4(b) shows the calculated results for $\gamma_{rad,uni}$, $\gamma_{rad,bi}$, $\gamma_{abs,uni}$, and $\gamma_{abs,bi}$ as a function of *g*. The rates $\gamma_{abs,uni}$ and $\gamma_{abs,bi}$ are constant around 0.13 THz and 0.17 THz, respectively, while $\gamma_{rad,uni}$ and $\gamma_{rad,bi}$ depend strongly on *g*.

#191484 - $15.00 USD Received 5 Jun 2013; revised 19 Sep 2013; accepted 11 Oct 2013; published 22 Oct 2013

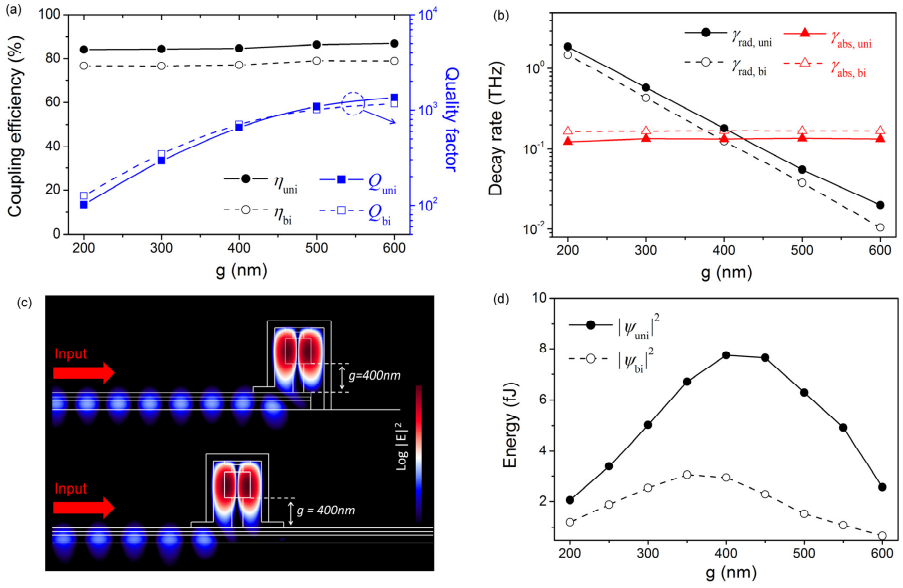

Fig. 4. (a) Coupling efficiencies η_{uni} and η_{bi} and quality factors Q_{uni} and Q_{bi} as a function of g for structures of Figs. 3(e) and 3(b), respectively. (b) Radiation rates $\gamma_{rad,uni}$ and $\gamma_{rad,bi}$ and absorption rates $\gamma_{abs,uni}$ and $\gamma_{abs,bi}$ of cavity modes in panel (a) as a function of g, respectively. (c) Profile of E^2 on logarithmic scale along x-z plane for unidirectional and bidirectional cases for g = 400 nm when light is coupled from waveguide. (d) Total energies $|\psi_{uni}|^2$ and $|\psi_{bi}|^2$ inside cavity for 10-mW waveguide input as a function of g.

Based on the observations summarized in Figs. 4(a) and 4(b), we use coupled-mode theory to analytically express the total energy ($|\psi_{uni}|^2$ or $|\psi_{bi}|^2$) for unidirectional and bidirectional cases, respectively) in the cavity when light couples from the integrated waveguide with the same definitions in [29]:

$$\frac{d\psi_i}{dt} = j\omega_i\psi_i - \frac{1}{2}\left(\gamma_{rad,i}(g) + \gamma_{abs,i}\right)\psi_i + \sqrt{\xi\,\gamma_{waveguide,i}(g)}\; s_{input}. \qquad (1)$$

Here, the subscript i = "uni" or i = "bi" for the unidirectional or bidirectional cases, respectively. The quantity ω_i is the resonant frequency of the cavity mode, and $|s_{input}|^2$ represents the input power from the waveguide. The constant ξ = 1 or 1/2 for unidirectional or bidirectional, respectively. We assume that $\gamma_{rad,i}$(g) and $\gamma_{waveguide,i}$(g) vary as a function of g; $\gamma_{abs,i}$ is a constant estimated from Fig. 4(b).

From the definition of coupling efficiency (η_i = $\gamma_{waveguide,i}$ / $\gamma_{rad,i}$), $\gamma_{waveguide,i}$(g) can be replaced by $\eta_i \cdot \gamma_{rad,i}$(g) and, based on the results shown in Fig. 4(a), η_i can be regarded as a constant for 200 nm < g < 600 nm. Thus, from Eq. (1), the steady-state total cavity energy $|\psi_i|^2$ at the resonant frequency ω_i is

$$|\psi_i|^2 = 4\eta_i\,\xi\,\frac{\gamma_{rad,i}(g)}{\left(\gamma_{rad,i}(g) + \gamma_{abs,i}\right)^2}\left|s_{input}\right|^2. \qquad (2)$$

Equation (2) shows that the total cavity energy follows $\gamma_{rad,i}$(g) / ($\gamma_{rad,i}$(g) + $\gamma_{abs,i}$)^2 and is maximized when the condition $\gamma_{rad,i}$(g) = $\gamma_{abs,i}$ is satisfied. From Eq. (2), the maximum energy in the cavity under optimized conditions is $|\psi_i|^2 = (\eta_i \cdot \xi / \gamma_{rad,i})|s_{input}|^2$. Note that the energy in the cavity is proportional to the coupling efficiency η_i and inversely proportional to the total cavity-to-radiation rate $\gamma_{rad,i}$. In addition, the value of ξ for $|\psi_{uni}|^2$, which is 1, is twice as large as its counterpart for$|\psi_{bi}|^2$.

#191484 - $15.00 USD Received 5 Jun 2013; revised 19 Sep 2013; accepted 11 Oct 2013; published 22 Oct 2013

Figure 4(b) indicates that $g \approx 400$ nm is optimal (or, more accurately, $g = 380$ nm and 430 nm for the unidirectional and bidirectional cases, respectively) because $\gamma_{rad,i}$ matches $\gamma_{abs,i}$ for this value. Figure 4(c) shows the intensity distribution of the electric field on a logarithmic scale in the x-z plane when $g = 400$ nm for the unidirectional and bidirectional cases, where the light enters from the left end of the waveguide. This figure clearly shows that the energies inside the cavities are highly coupled from the waveguide inputs. Figure 4(d) shows the simulated total energies in the III-V cavities for 10-mW input as a function of g for the unidirectional and bidirectional cases. This result implies that the energies in the cavities are maximized when $\gamma_{rad,i}$ matches $\gamma_{abs,i}$ [Fig. 4(b)] and the optimized $g \approx 380$ nm and 430 nm for the unidirectional and bidirectional cases, respectively. The maximum cavity energies for 10-mW input are calculated to be 7.7 and 3.0 fJ for the unidirectional and bidirectional cases, respectively, where the smaller energy in the bidirectional case is attributed to the 50% value of ξ and the slightly lower coupling efficiency ($\eta_{bi} < \eta_{uni}$). As the result indicates, controlling the height g of the bottom-cladding layer in the metal-clad nanocavity proves to be a simple and highly effective way to optimize the optical coupling into the integrated Si waveguide and to thereby maximize the cavity energy.

7. Summary

We have shown that cladding engineering for the metal-clad nanocavity is a flexible approach to modify the radiation patterns and rates of cavity modes and greatly enhances coupling with integrated waveguides, thereby maximizing the standing energy inside the cavity. We believe this method will prove to be fundamental and important tool in developing next-generation optical communication devices.

Acknowledgments

The authors thank Dr. Se-Heon Kim for helpful discussions. This work was supported by the Engineering and Applied Sciences (EAS) division of the California Institute of Technology and the Powell Foundation.